

Multi-objective Bayesian Optimization with Human-in-the-Loop for Flexible Neuromorphic Electronics Fabrication

Supplementary Information

Benius Dunn,^a Javier Meza-Arroyo,^b Armi Tiihonen,^b Mark Lee ^c and Julia W. P. Hsu ^{*ac}

^a Department of Materials Science and Engineering, The University of Texas at Dallas, Richardson, Texas 75080, USA

^b Department of Applied Physics, Aalto University, Espoo, Finland

^c Department of Physics, The University of Texas at Dallas, Richardson, Texas 75080, USA

*Corresponding author. Email: jwhsu@utdallas.edu

Initial Latin hypercube sampling (LHS) photonic curing conditions

Table S1. Ranges and step sizes for LHS sampling

Variable Name	Minimum Value	Maximum Value	Step Size	Number of steps
Radiant Energy (J/cm ²)	1.0	7.0	0.2	31
Pulse Count	1	20	1	20
Pulse Length (ms)	1	20	1	20
Number of Micropulses	1	30	1	30
Duty Cycle (%)	20	70	5	11

Table S2. Photonic curing input parameters, human observation scores, and measured device outputs for initial LHS conditions. Data for all conditions is available through [UTD-Hsu-Lab/ParetoUCB](#).

Condition #	Radiant Energy (J/cm ²)	Pulse Count	Pulse Length (ms)	Micropulse Count	Duty Cycle (%)	Pulse Voltage (V)	Conversion Score (-1 – 1)	C_{100Hz}/C_{1MHz}	$ \log(I_{leakage}) $
1	1.4	5	19	22	45	216	-1.0	-	-
2	3.8	8	5	12	35	447	1.0	-	-
3	3.2	4	4	19	30	492	1.0	-	-
4	6	14	3	13	20	810	1.0	-	-
5	5.4	9	19	17	40	374	1.0	-	-
6	4.4	17	10	6	25	418	1.0	-	-
7	3	7	17	7	25	323	1.0	-	-
8	6.6	12	2	15	50	651	1.0	-	-
9	2.4	1	13	1	65	256	-1.0	-	-
10	2	18	8	10	45	290	-0.5	2.00 ± 0.23	1.09 ± 0.69
11	6.8	17	2	5	30	766	1.0	-	-
12	3.4	6	12	9	40	330	1.0	-	-
13	1	14	14	25	60	190	-1.0	-	-
14	6.2	20	6	16	55	450	1.0	-	-
15	1.6	3	15	4	55	220	-1.0	-	-
16	4.8	16	7	26	65	385	0.5	1.19 ± 0.08	4.90 ± 0.27
17	4.2	4	9	23	70	344	0.0	1.58 ± 0.20	3.96 ± 0.38
18	2.8	10	11	29	50	305	-0.5	2.10 ± 0.40	3.55 ± 0.22
19	5.8	11	18	27	60	371	0.5	2.30 ± 0.43	3.46 ± 0.43
20	5	13	15	21	35	388	0.0	2.27 ± 0.43	3.07 ± 0.23
21	3.8	6	10	27	25	426	0.0	2.36 ± 0.49	3.44 ± 0.40
22	3.2	7	12	21	45	322	-0.5	3.30 ± 0.42	3.30 ± 0.17
23	5.8	9	17	10	40	388	1.0	-	-
24	1.8	2	8	23	50	271	-1.0	-	-
25	5.2	6	10	30	55	388	0.5	2.00 ± 0.29	0.88 ± 0.97
26	2.6	10	8	15	70	288	0.0	2.50 ± 0.40	3.88 ± 0.23
27	1.8	8	4	25	30	412	-1.0	-	-
28	2.4	4	20	17	65	252	-1.0	-	-
29	1.2	3	3	5	35	346	-1.0	-	-
30	4.4	3	18	3	20	382	1.0	-	-

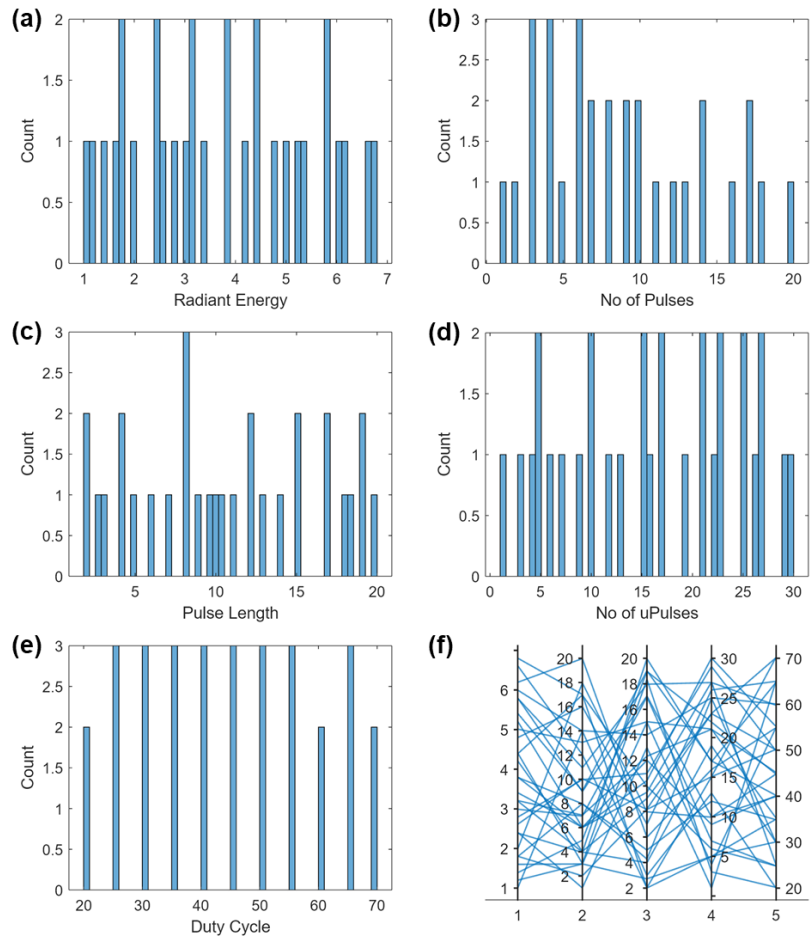


Fig. S1. Histograms showing distribution of initial LHS photonic curing parameters (a) radiant energy, (b) number of pulses, (c) pulse length, (d) number of micropulses, and (e) duty cycle. (f) Parallel plot for all 30 initial LHS conditions across all five input parameters to demonstrate exploration across the entire input space.

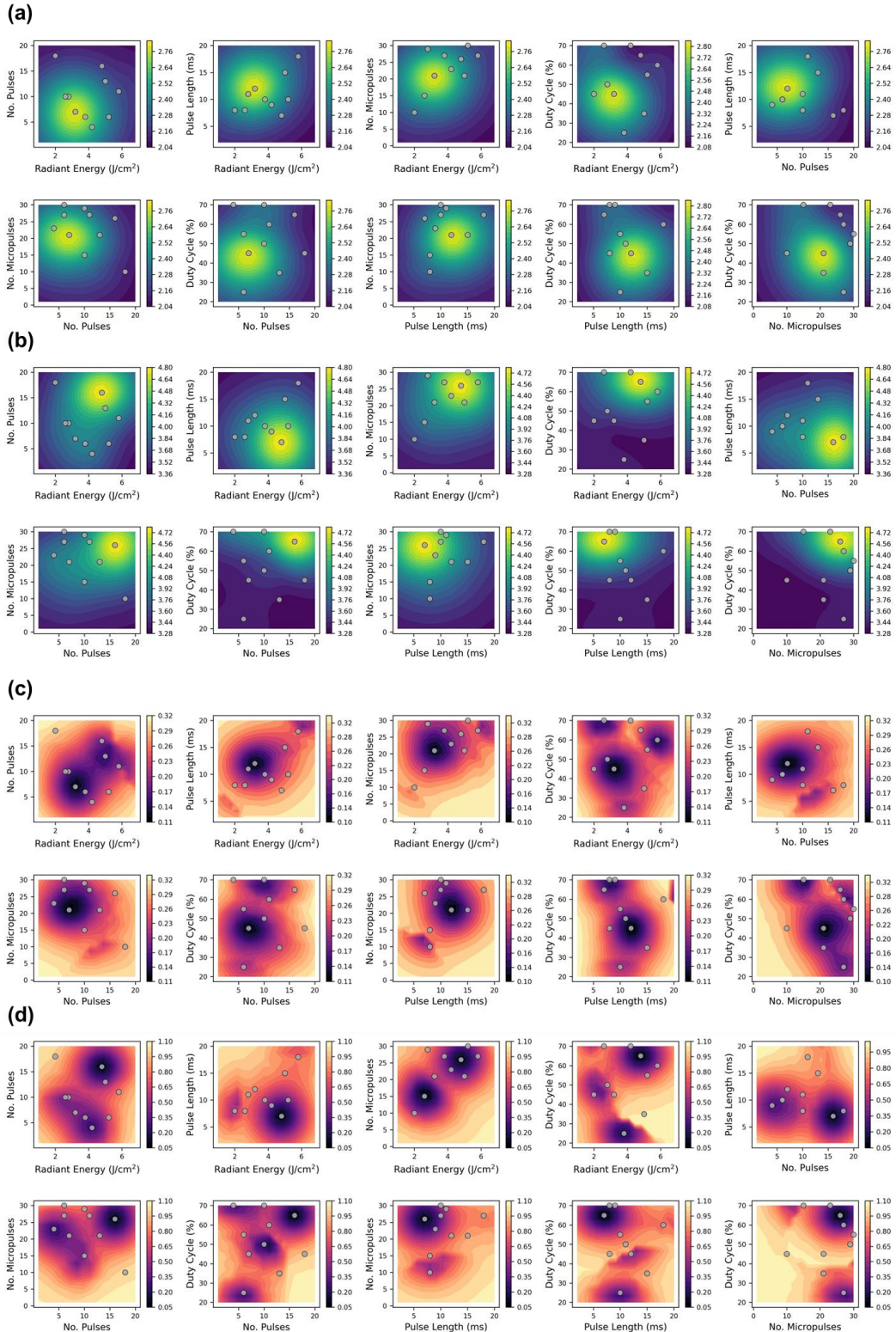


Fig. S2. GPR models built from the data collected on functional devices made with initial 30 LHS conditions: posterior mean of (a) C-f dispersion (C_{100Hz}/C_{1MHz}), and (b) leakage current ($|\log(I_{leakage})|$); variance of (c) C-f dispersion, and (d) leakage current.

Human-in-the-Loop methodology

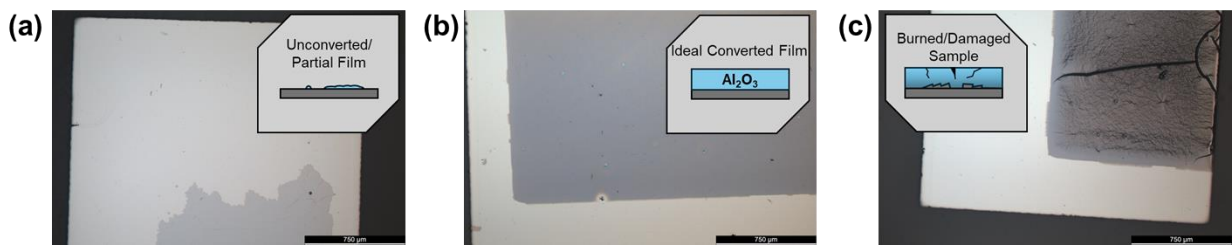
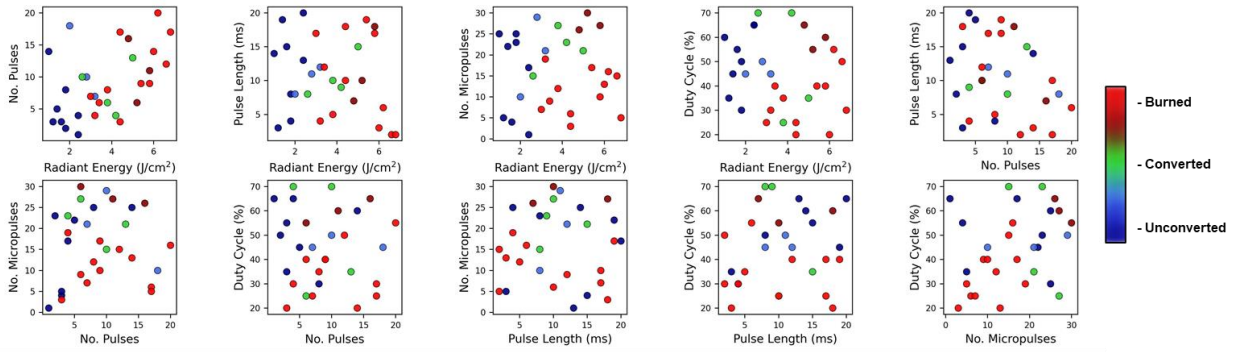
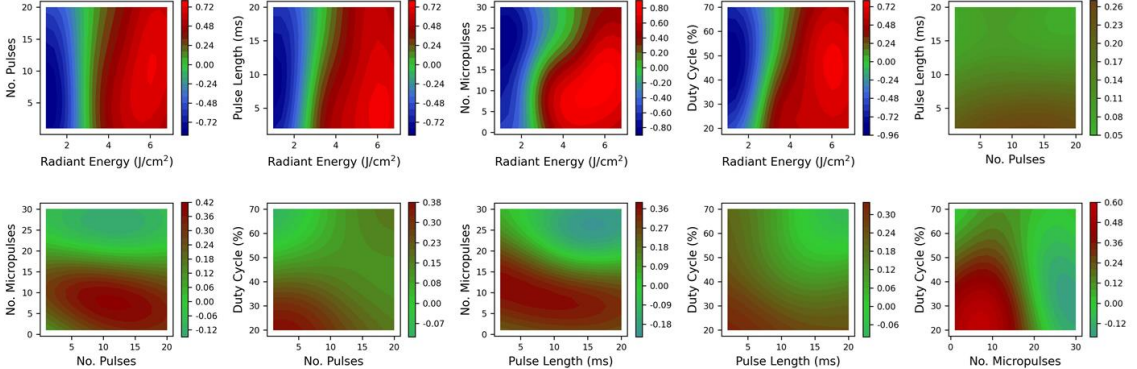


Fig. S3. Optical microscope images of films after photonic curing showing different conversion outcomes: (a) under-converted film with partial film remaining, (b) good conversion that can result in functional devices, and (c) burned sample.

(a)



(b)



(c)

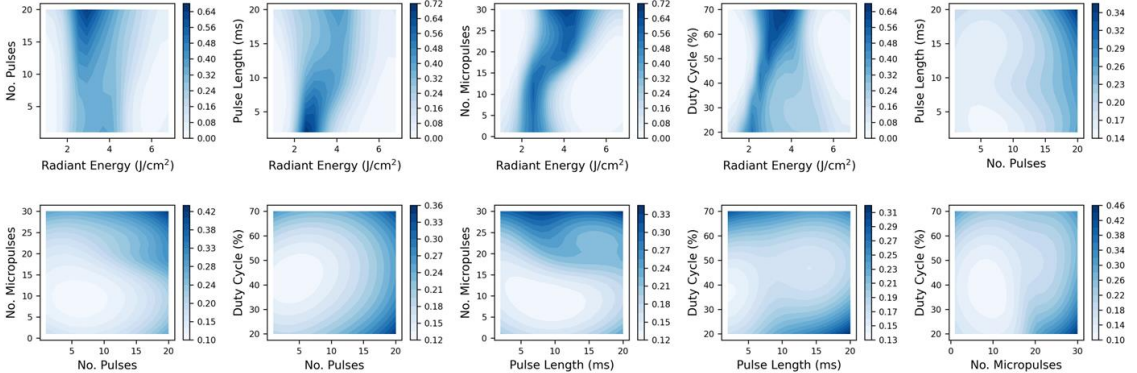


Fig. S4. (a) Human observation scores of the initial 30 LHS conditions, (b) GPR model trained on human observation scores, and (c) resulting HITL probability distribution $P_{constraint}$ obtained from a Gaussian transformation of (b).

Dominated hypervolume evolution & final GPR models' accuracy

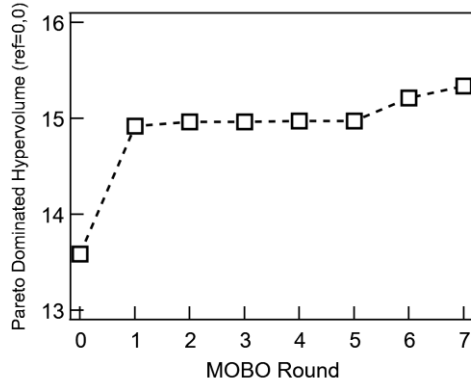


Fig. S5. Dominated hypervolume by Pareto optimal data points across each round of MOBO, starting with initial LHS (round 0)

When using a machine learning model as a surrogate for real experimental data, fitting is often less ideal than with synthetic data due to sample-to-sample variation and limited availability of data points for model training. As depicted in Fig. S6(a), after completing all MOBO rounds, the final GPR model for C-f dispersion tends to overestimate values of C_{100Hz}/C_{1MHz} for values greater than ~ 2 . However, the region of feasible device fabrication is limited to values of C_{100Hz}/C_{1MHz} less than 2, for which the model shows suitable accuracy. The final GPR model of leakage current similarly shows reasonable accuracy for the region of feasible device fabrication with values of $|\log(I_{leakage})| \geq 4$ in Fig. S6(b). The C-f dispersion model has a linear fit slope of 0.723 with a R^2 value of 0.938. The leakage current model has a linear fit slope of 0.852 with a R^2 value of 0.964.

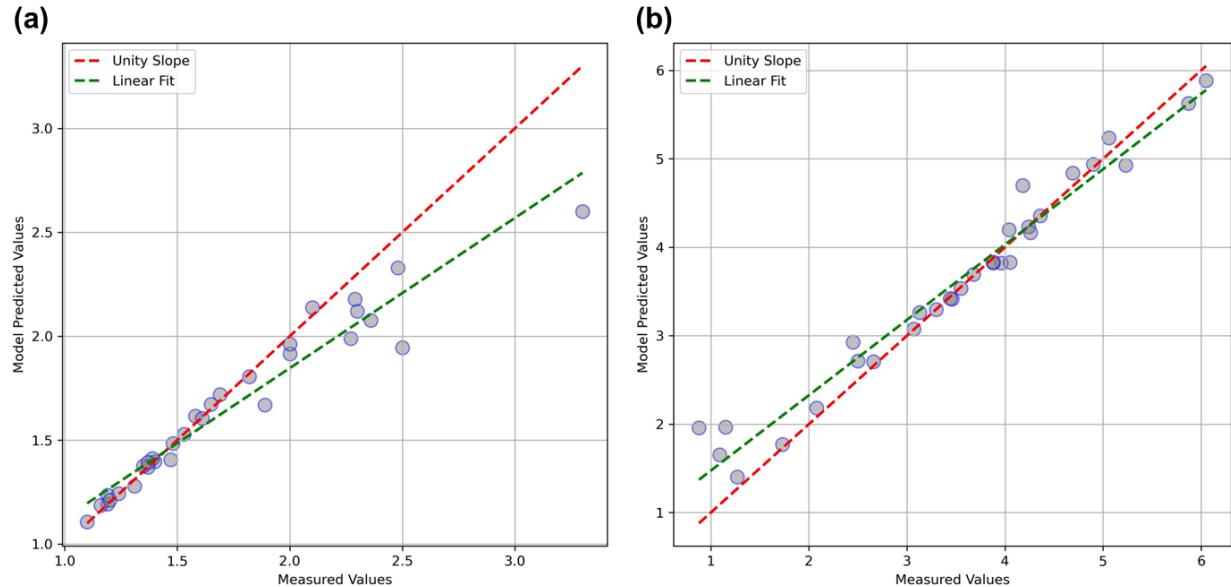


Fig. S6. Final GPR model predictions versus measured output values for (a) C-f dispersion (C_{100Hz}/C_{1MHz}), and (b) leakage current ($|\log(I_{leakage})|$).

Physical and chemical property comparison of dielectrics from MOBO conditions #40 and #66

Conditions #40 and #66 represent the two extreme conditions along the Pareto frontier within the realm of feasible device fabrication ($I_{\text{leakage}} < 10^{-4} \text{ A/cm}^2$). This section compares the processing conditions and the physical and chemical properties of Al_2O_3 dielectrics made using these two conditions. Fig. S7 shows simulated temperature profiles over time for a single photonic curing pulse under conditions #40 and #66. The temperature profiles are constructed using the SimPulse® photonic curing simulation software, which is included with the PulseForge Invent system. Samples are modeled as a material stack that consists of 100 μm PET, 100 nm aluminum metal, and 70 nm Al_2O_3 . Profiles are generated in surface absorption mode with 11% surface absorption, which is determined using a NIST-calibrated bolometer to estimate transmission % and reflectance mode UV-vis to estimate reflectance %. Profiles for the top of the Al_2O_3 in Fig. S7(a) show the sample processed with condition #40 reaching a peak temperature of 159°C, while the sample under condition #66 reaches a lower peak temperature of 127°C. For both conditions, the bottom of the PET substrate does not exceed 55°C, as shown in Fig. S7(b). While the one-dimensional thermal model is very simple, the difference in peak temperature of the film suggests that condition #40 induces a greater conversion from precursor to oxide dielectric.¹

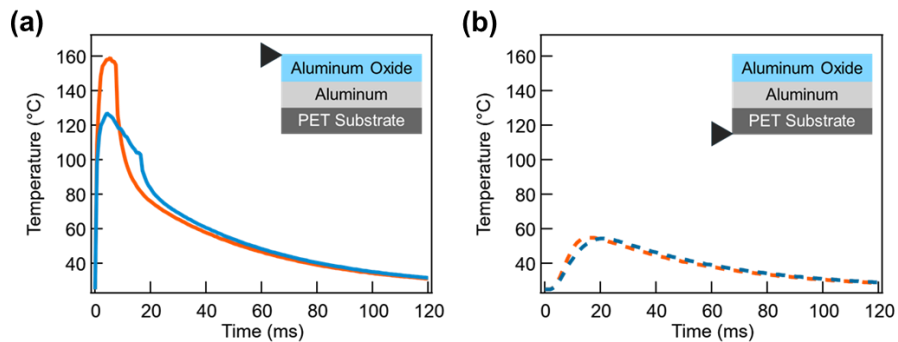


Fig. S7. SimPulse® simulated temperature profiles for a single pulse of MOBO conditions #40 (orange) and #66 (blue) (a) on the Al_2O_3 film surface and (b) at the bottom of the PET substrate.

We further investigate the chemical difference between the films after photonic curing by X-ray photoelectron spectroscopy (XPS) to study the conversion outcome. XPS is performed on a Ulvac-PHI VersaProbe2 with a monochromated Al K α source (1486.8 eV) at an angle of 45° to the sample surface. O1s spectra are averaged over 20 scans with an energy step of 0.2 eV and a pass energy of 23.5 eV. N1s spectra are averaged over 100 scans with an energy step of 0.2 eV and a pass energy of 187.85 eV. Fitting is performed with the CasaXPS software using a mixed 30:70 Gaussian:Lorenzian functions for all peaks, and binding energy is calibrated using the 284.8 eV C1s peak from adventitious carbon.

O1s spectra are fit to two peaks reflecting the different chemical environments of oxygen within the dielectric: 530.4 eV peak corresponding to metal oxide and 532 eV peak corresponding to metal hydroxide. Dielectric fabricated using condition #40 shows a metal oxide signal of 19% (Fig. S8(a)) while the one fabricated using condition #66 only has a metal oxide signal of 6.7% (Fig. S8(b)), in line with the expectation that the film reaches a higher temperature under condition #40 and has a greater conversion to metal oxide.

Also shown in Fig. S8(c) is the N1s signal intensity at 407 eV for each sample. This N1s signal arises primarily from residual nitrate (NO_3^-) from the aluminum nitrate precursor. As such, the lower N1s signal present from condition #40 provides further evidence of greater conversion from precursor to metal oxide. This analysis is consistent with the expected behavior of the simulated temperature profiles in Fig. S7.

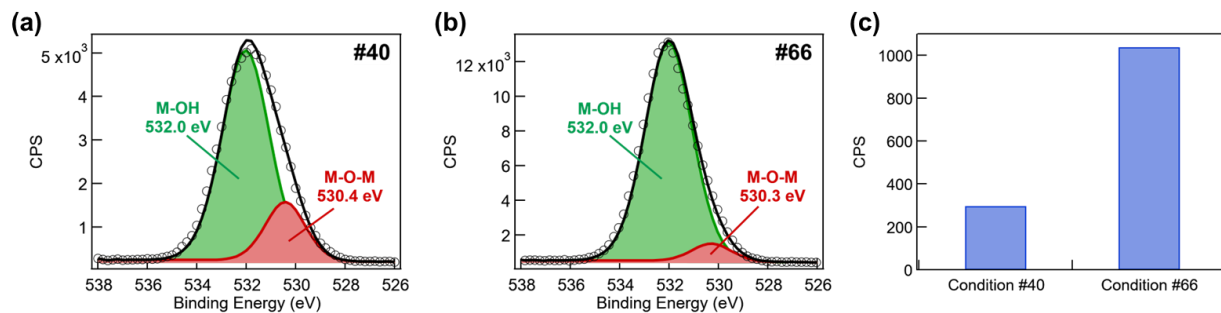


Fig. S8. XPS O1s spectra for (a) MOBO condition #40 and (b) #66. (c) XPS N1s peak intensity comparison for conditions #40 and #66.

HITL methodology comparison data and summary of methods used for each round of MOBO

The acquisition functions used in each round of MOBO, as well as whether the HITL methodology is implemented, are indicated in Table S4. Rounds 1a and 1b are both picked by the models trained on the 10 successful devices from the 30 LHS conditions only, their only difference being the acquisition function used. Thus, round 2 begins once the model is updated with the data from rounds 1a and 1b. Rounds 1' and 2' are the picks by models constrained with HITL knowledge (Fig. 4(c)). Round 1' is trained only on the results of the initial 30 LHS conditions, while round 2' is trained on the updated model with data from LHS and round 1'.

Table S4. Conditions for each round of multi-objective optimization: acquisition function used (qEHVI: parallel expected hypervolume improvement; ParUCB: Pareto-UCB batch picking), and whether human-in-the-loop (HITL) is used in each round.

Round #	1a	1b	2	3	4	5	6	7
Acquisition Function	qEHVI	ParUCB	qEHVI	qEHVI	qEHVI	qEHVI	ParUCB	ParUCB
HITL	✗	✗	✗	✓	✓	✓	✓	✓

Round #	1'	2'
Acquisition Function	ParUCB	ParUCB
HITL	✓	✓

Table S5. Photonic curing input parameters, human observation scores, and measured device outputs for rounds of HITL methodology comparison.

Round #	Condition #	Radiant Energy (J/cm ²)	Pulse Count	Pulse Length (ms)	Micropulse Count	Duty Cycle (%)	Pulse Voltage (V)	Conversion Score (-1 – 1)	C _{100Hz} /C _{1MHz}	log(I _{leakage})
1a	31	2.7	8	11	18	54	294	-1.0	-	-
1a	32	3.1	6	13	21	37	328	-1.0	-	-
1a	33	3.4	12	8	20	70	322	0.0	1.53 ± 0.15	2.50 ± 0.39
1a	34	2.4	5	8	14	70	280	-1.0	-	-
1a	35	3.3	9	14	21	47	315	-1.0	-	-
1b	36	2.8	8	11	20	52	301	-1.0	-	-
1b	37	3	8	11	21	45	320	-1.0	-	-
1b	38	4	14	8	21	70	345	0.0	1.19 ± 0.12	5.23 ± 0.50
1b	39	4.3	14	8	22	67	357	0.0	1.16 ± 0.15	5.87 ± 0.30
1b	40	4.5	16	7	23	70	369	0.5	1.10 ± 0.04	6.05 ± 0.24
2	41	2.4	6	12	20	43	292	-1.0	-	-
2	42	4	7	12	20	43	354	-1.0	-	-
2	43	4.4	17	11	21	65	346	0.0	1.40 ± 0.07	4.18 ± 1.05
2	44	3	4	13	26	39	322	-1.0	-	-
2	45	2.1	6	9	12	66	262	-1.0	-	-
1'	31'	3.7	14	13	20	70	314	0.0	2.76 ± 0.61	3.44 ± 0.13
1'	32'	2.9	1	13	18	37	320	-1.0	-	-
1'	33'	3.3	15	9	26	70	315	0.0	2.93 ± 0.36	2.99 ± 0.27
1'	34'	3.3	6	12	18	40	336	0.0	1.98 ± 0.22	3.44 ± 0.80
1'	35'	3.7	10	15	15	67	311	0.0	2.60 ± 0.46	3.24 ± 0.14
2'	36'	2.9	6	6	20	70	321	0.0	2.09 ± 0.16	3.23 ± 0.73
2'	37'	3.3	11	10	18	60	319	0.0	3.15 ± 0.69	3.13 ± 0.25
2'	38'	4.5	17	13	28	57	352	0.0	1.46 ± 0.11	4.30 ± 0.24
2'	39'	2.9	9	7	20	63	320	0.0	2.52 ± 0.34	3.29 ± 0.13
2'	40'	3.3	15	10	20	63	316	0.0	2.23 ± 0.27	3.04 ± 0.60

SHAP analysis scatter plots for individual input variables

The dependencies of SHAP values on photonic curing parameter input values are depicted by scatter plots for the C-f dispersion model (Fig. S9) and leakage current model (Fig. S10). A positive correlation between SHAP value and input parameter value, such as for pulse length in Fig. S9(c), indicates that increasing this input will increase the output of the model. Conversely, a negative correlation between SHAP value, such as for radiant energy in Fig. S9(a), indicates that increasing this input will decrease the output of the model.

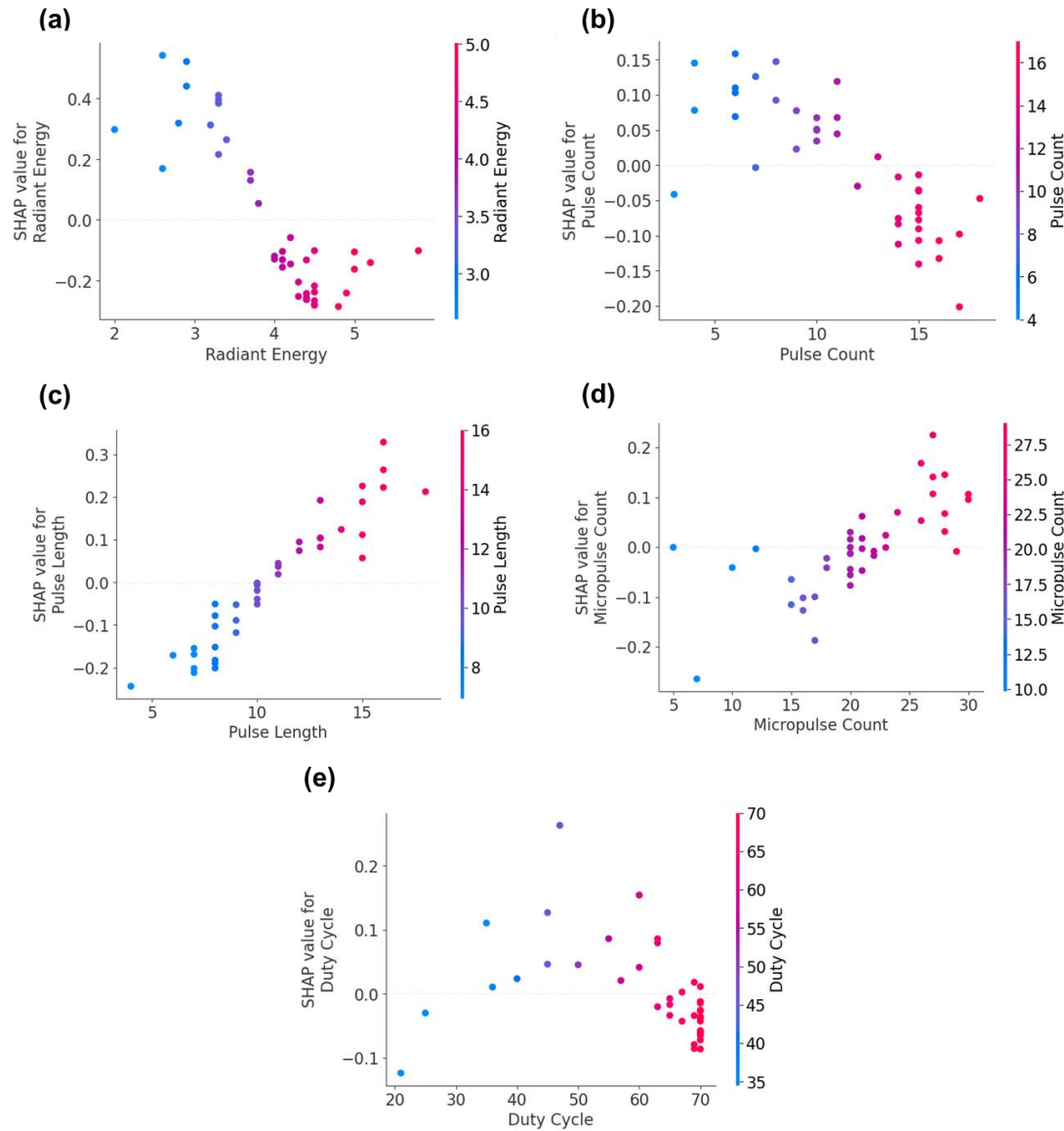


Fig. S9. SHAP values of C-f dispersion (C_{100Hz}/C_{1MHz}) model versus input values for (a) radiant energy, (b) pulse count, (c) pulse length, (d) micropulse count, and (e) duty cycle.

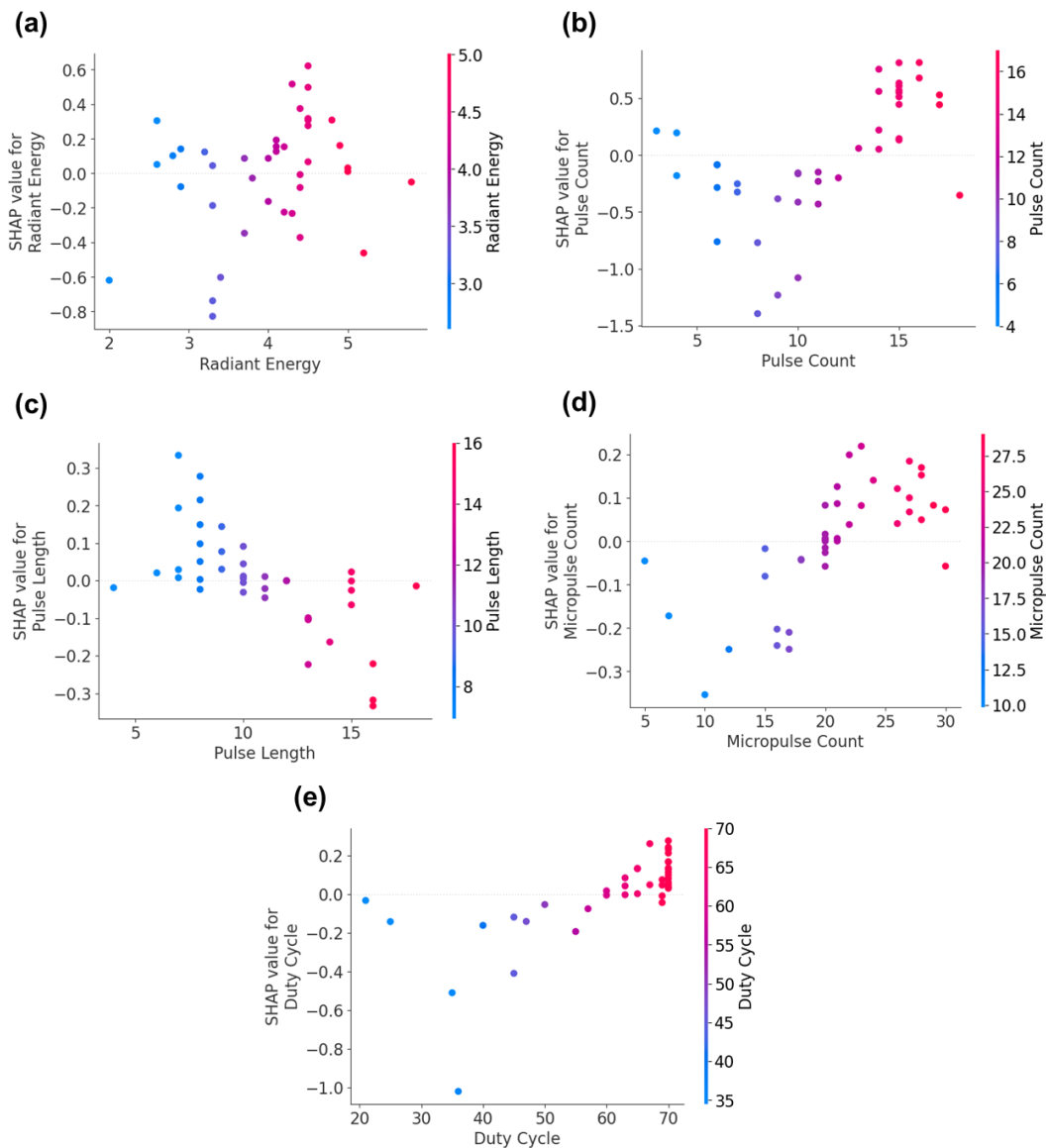


Fig. S10. SHAP values of leakage current ($|\log(I_{\text{leakage}})|$) model versus feature values for (a) radiant energy, (b) pulse count, (c) pulse length, (d) micropulse count, and (e) duty cycle.

References

- 1 E. A. Cochran, K. N. Woods, D. W. Johnson, C. J. Page and S. W. Boettcher, *J Mater Chem A Mater*, 2019, **7**, 24124–24149.